

---

## GEOMETRIC CALIBRATION OF THE MICAS CCD SENSOR ON THE DS1 (DEEP SPACE ONE) SPACECRAFT: LABORATORY VS. IN-FLIGHT DATA ANALYSIS

Jürgen OBERST, Bärbel BRINKMANN, Bernd GIESE

German Aerospace Center (DLR), Institute of Space Sensor Technology and Planetary Exploration  
Berlin, Germany

[Juergen.Oberst@dlr.de](mailto:Juergen.Oberst@dlr.de)

Working Group IC - 4

**KEY WORDS:** CCD, Camera, Calibration

### ABSTRACT

We have carried out a geometric calibration of the CCD sensor of MICAS (Miniature Integrated Camera Spectrometer), a 4-inch aperture reflecting telescope on board the DS1 (Deep Space One) spacecraft, using laboratory data and in-flight images of star fields. The images suffer from significant distortion up to 4 pixels near the margins, an effect which we modelled by two-dimensional polynomials of 10th degree. The focal length of the camera is determined to be  $f = 686.55 \pm 0.05$  mm, clearly above the nominal design value. In-flight images show that the geometric properties of the camera essentially have not changed. Following image geometric corrections on the basis of the laboratory data, positions of stars in the images can be predicted to within 0.5 pixels ( $1 \sigma$ ). The analysis demonstrates that ground calibration data which can be obtained and processed very rapidly constitutes an important basis for the evaluation of camera geometric properties.

### I INTRODUCTION

The DS1 (Deep Space One) spacecraft was launched on October 24, 1998 from Cape Canaveral Air Station, FL. This mission is part of the New Millennium program of NASA, which has the goal to test new technologies for future space and Earth-observing missions [Nelson, 1998; Nelson et al., 2000]. The spacecraft encountered the 2-km asteroid Braille on July 28, 1999 and is now on a trajectory to an encounter with the comet Borrelly in September 2001.

DS1 is equipped with an onboard camera for imaging of the flyby targets. The camera is also used to support the navigation of the spacecraft. The onboard flight software (one of several technology experiments of DS1) is intended to measure positions of solar system objects relative to the background stars with the goal to autonomously determine the spacecraft's position and trajectory. For precise navigation, it is absolutely required that the imaging sensor is geometrically calibrated precisely. An effort was therefore made by members of the DS1 science and navigation teams to study the geometric performance of this sensor, specifically, to find algorithms to correct for possible image distortion

### 2 MICAS CAMERA AND CCD SENSOR

The spacecraft camera, MICAS (Miniature Integrated Camera Spectrometer, Fig. 1), combines the functionality of a framing camera with that of an imaging spectrometer. Two array sensors (briefly termed "APS" and "CCD") with two spectrometers ("UV" and "IR") share one common 4-inch aperture optical system. The "CCD" array sensor with a size of 1024 x 1024 pixels, and a nominal focal length of 677 mm (Table 1) is the prime instrument to obtain frame images. Owing to the compact design of the camera, the light path is complicated (Fig. 1, right).

### 3 LABORATORY DATA

Comprehensive laboratory studies of camera performance were carried out at JPL (Jet Propulsion Laboratory) in summer 1998, before the camera was mounted on the spacecraft. These included evaluations of the geometric properties of images obtained by the CCD sensor. Images of a geometric calibration target, placed in a collimator, were taken. The target, made photolithographically to high accuracy, shows a 5 x 5 pattern of "holes" which were very nearly equally spaced (Fig. 2). The target was initially centered in the field of view, then shifted to the upper left, top, upper right, lower left, bottom, lower right. Finally, the target was turned by 90°. Multiple exposures at each target position were taken; three sets of exposures, 21 images, were finally used in this analysis.

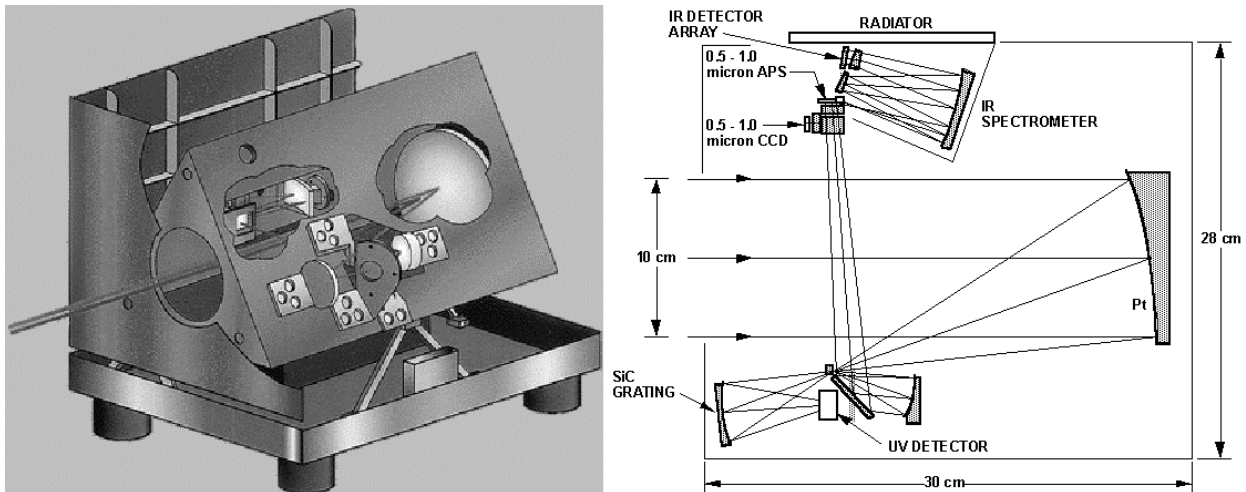


Fig. 1: The MICAS camera (left) and the optical light path. Four sensors share one optical system (see text and Table 1 for details).

Table 1: MICAS Optics First Order Properties

	UV	VIS(APS)	VIS(CCD)	IR
Wavelength, nm	80-185	500-1000	500-1000	1200-2400
Focal Length, cm	17.1	67.7	67.7	75.2
Detector Array	35 x 164	256 x 256	1024 x 1024	256 x 256
Pixel Size,	54	12.0	9.0	40
FOV, °	0.63 x 0.03	0.26 x 0.26	0.69 x 0.78	0.7 x 0.003

#### 4 APPROACH

The apparent line/sample positions of the grid holes in MICAS images were measured. It was assumed that the holes were all equally spaced and that images of the grid differed only by relative lateral shifts and small rotations. Best-fit shift and rotation parameters for each grid, as well as the grid hole spacing were determined from the measurements using iterative least-squares methods. This procedure was repeated for the 7 target positions. Fig. 3 (left) shows the residuals (i.e. the difference between measured position of the grid holes and the position as predicted by the model), all 7 target positions added, after the fit. The residuals scatter by 0.65–1.04 pixels ( $1 \sigma$ ) for individual images, with peak magnitudes of the residuals being up to 4 pixels near the image margins. This is well beyond measurement errors (estimated to be  $< 1$  pixel) and therefore suggests that significant image distortion must be present. From the known precise grid hole spacings of the target (Table 2), we estimate that the focal length is  $f = 686.55 \pm 0.05$  mm (mean of all fits).

One may wonder if this pattern seen in the image is perhaps due to the grid's lack of perfection. Fortunately, the object coordinates of the holes in the target had been explicitly measured in the collimator (Table 2), which allowed us (not only to determine the absolute focal length of the camera but also) to verify if the target was suited for this type of calibration approach. The object coordinates were projected to the image plane of the camera adopting the nominal focal length. This resulted in sets of synthetic line/sample coordinates of the holes, which were subjected to the same inversion procedure as described above. The residuals show random scatter with  $\sigma = 0.101$  pixels, which demonstrates the high geometric quality of the grid, more than sufficient for our calibration approach. It also becomes clear that the distortion pattern seen in the real grid images must be due to an effect caused by the MICAS optical system.

Table 2: Angular Coordinates of 5 x 5 grid holes in object space of collimator in degrees

91.63145	89.60811
91.76949	89.60704
91.90728	89.60579
92.04538	89.60463
92.18328	89.60350
91.63259	89.74619
91.77063	89.74497
91.90863	89.74376
92.04651	89.74271
92.18443	89.74157
91.63369	89.88405
91.77179	89.88303
91.90970	89.88176
92.04786	89.88063
92.18571	89.87943
91.63496	90.02232
91.77289	90.02112
91.91097	90.01995
92.04887	90.01881
92.18687	90.01766
91.63613	90.16020
91.77414	90.15910
91.91211	90.15795
92.05009	90.15661
92.18815	90.15540

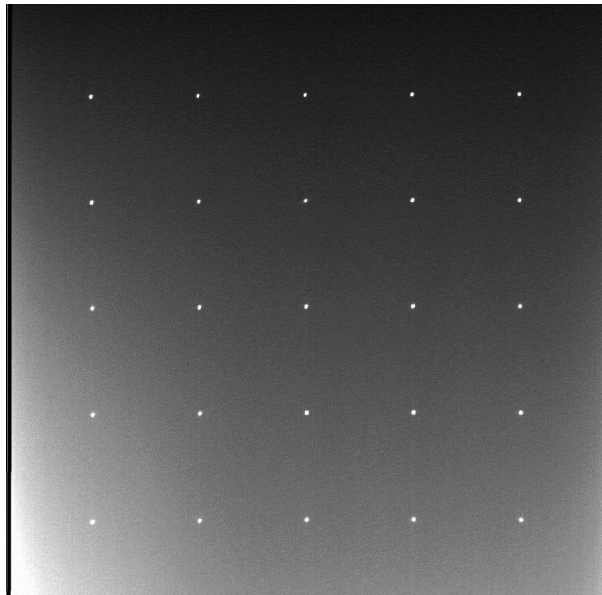


Fig. 2: The calibration grid used for laboratory geometric calibration of the MICAS CCD sensor.

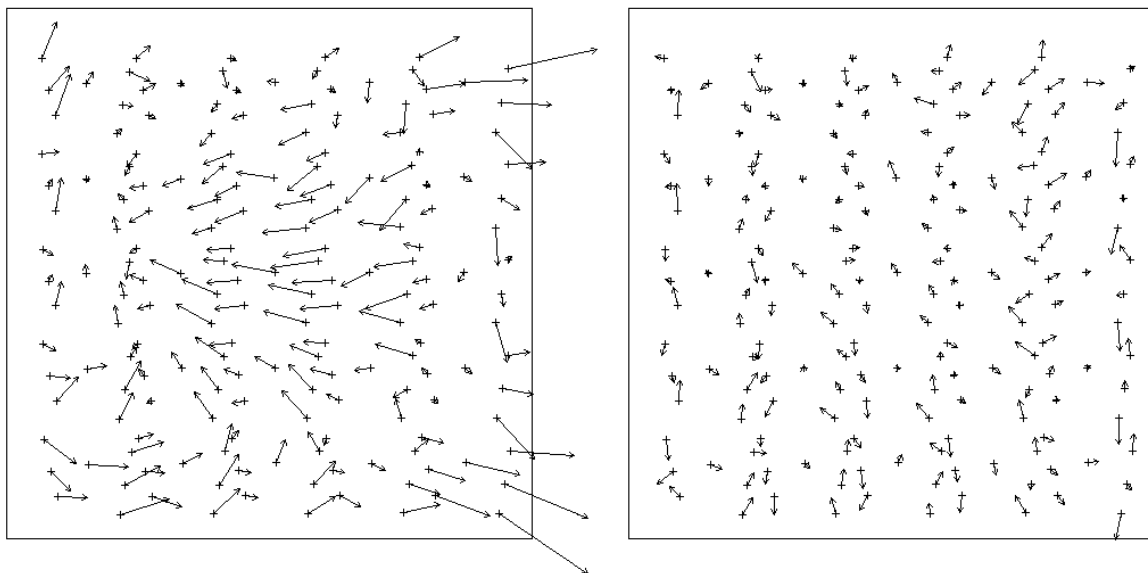


Fig. 3: Vector plots showing offsets between nominal and measured position of grid holes in the 1024 x 1024 image. Data from 7 grid images (from the total of 21 images used in this analysis) were combined. The plot shows data residuals before (left) and after (right) the best-fit distortion model (equations 1-3, Table 3) is applied. Note that the lengths of the arrows are exaggerated by a factor of 50. Hence, the distortions near the image margins before the correction (left) are as high as 4 pixels.

The line/sample residuals after the fit were modelled for image distortion by a 2-dimensional polynomial, assuming that the true line (l) and sample (s) positions of features in images can be expressed in terms of the nominal pixel position and some correction term which depends on the position in the image:

$$s_{true} = s_{nominal} + f_x(x,y) \qquad l_{true} = l_{nominal} + f_y(x,y) \qquad (1a, b)$$

with

$$\begin{aligned} f_x(x,y) = & a_1 + a_2*x & (2a) \\ & + a_3*y + a_4*x*x + a_5*y*y \\ & + a_6*x*y + a_7*x*x*y + a_8*y*y*x \\ & + a_9*x*x*x + a_{10}*y*y*y, \end{aligned}$$

$$\begin{aligned} f_y(x,y) = & b_1 + b_2*x & (2b) \\ & + b_3*y + b_4*x*x + b_5*y*y \\ & + b_6*x*y + b_7*x*x*y + b_8*y*y*x \\ & + b_9*x*x*x + b_{10}*y*y*y \end{aligned}$$

and

$$x = (s - 512.5) / 512 \qquad y = (l - 512.5) / 512 \qquad (3a, b)$$

All residual data from the individual fits were combined for the analysis. The polynomial model thus comprises 20 unknowns, which must be determined from the 1050 data points (3 exposures for each of 7 target positions; each image with 25 line- and 25 sample measurements). The solution can easily be obtained by inversion of the linear equations (Table 3). The residuals after the fit are significantly reduced from 0.828 to 0.354 pixels (1  $\sigma$ ); the total sum of squares before and after the fit are 718.6 and 131.6. Hence, the model can account for 81.7% of the scatter in the 1050 measurements. Tests (e.g. making model fits to parts of the data and testing the model on the rest of the data) show that the remaining residuals are probably due to random errors in the line/sample coordinate measurement (see Fig. 3, right). Therefore, it would not be meaningful to make fits using polynomials of higher order.

Table 3: Coefficients of Polynomial Model

i	a <sub>i</sub>	b <sub>i</sub>
1	-0.04575	-1.40084
2	-0.55665	-1.16967
3	-1.43470	-0.34597
4	0.35823	2.77181
5	-0.10251	2.31768
6	-0.05106	0.30575
7	0.05964	1.76965
8	1.95619	0.17784
9	1.59799	0.14735
10	0.24978	1.44159

## 5 IN-FLIGHT VERIFICATION OF THE DISTORTION MODEL

### 5.1 Star identification and line/sample coordinates

The distortion model was verified using in-flight images of star fields. 19 images were selected that each show 10-30 stars near the Praesepe star cluster (see Figs. 4,5 for an example). Positions of the stars were measured and compared with their nominal positions in the star PPM catalog (Positions and Proper Motions Roser and Bastian, 1989; Roser et al., 1991). Stars were often heavily smeared, showing trails with 5-30 pixels in length, depending on the image exposure times (see Fig. 4 for an example).

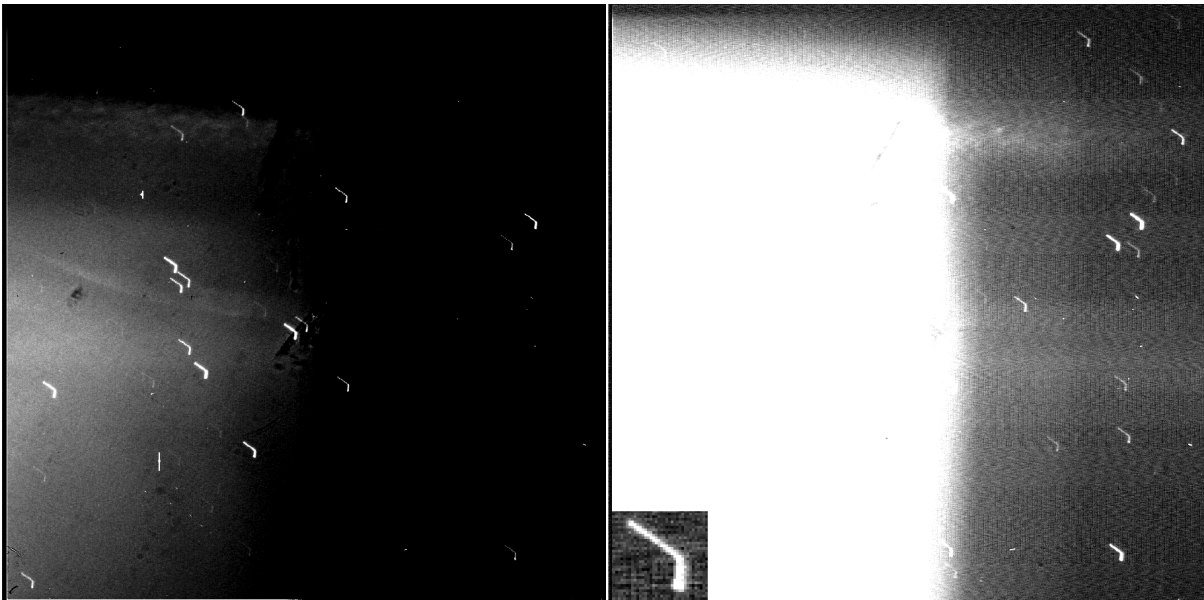


Fig. 4: Typical star image (starcl131) obtained by the MICAS CCD with two different stretches (left and right) being applied. The box at the lower left of the right image shows a magnified area around one of the stars, used as a "mask" for matching (see text for details). Scattered light problems make the firm identification of stars often difficult. Distinct star signatures as in this image actually help in the automated star position measurements.

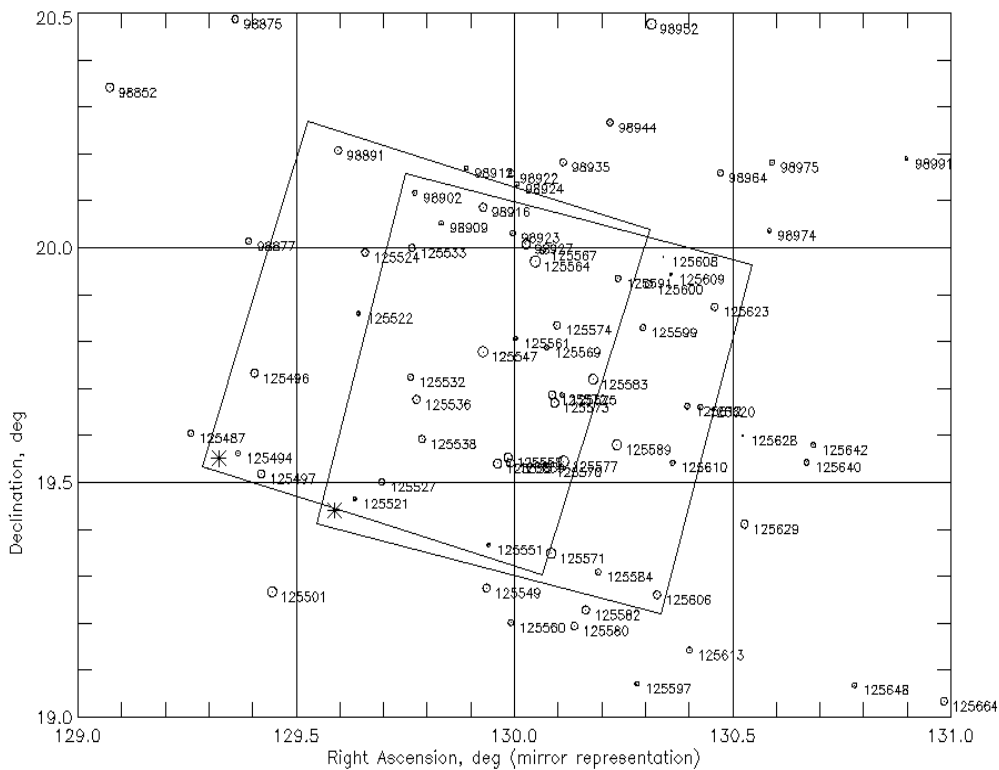


Fig. 5: Section of a star chart showing the positions of the images (right) starcl131 (see Fig. 4) and (left) nav04309. The stars mark the upper-left corner of the images. Note that MICAS images are mirrored! For that reason, the right ascensions are plotted to increase from left to right, opposite from what the naked eye would see in the sky.

A first attempt was made to measure the stars' positions manually. This was accomplished using an appropriate tiepoint program which allowed us to make the line/sample measurements at sub-pixel level. Stars seen in the in images were correlated with known stars by comparison with charts and catalogs.

Next, the star identifications and position measurements were made automatically. For this purpose, an image area  $m_{ij}$  having the size, for example, of  $i=20 \times j=20$  pixels around some "pilot" star was extracted and placed into a mask. Subsequently, the entire image was scanned for windows  $w_{ij}$ , to match this particular pattern. A star identification was considered to be acceptable, when the cross correlation coefficient  $c$ , given by the expression  $c = c_0 / \sqrt{c_1} / \sqrt{c_2}$ , exceeded a fixed value, e.g. 0.5, for a given window  $w_{ij}$  of the image.  $c_0$ ,  $c_1$ , and  $c_2$  were then computed by multiplication of corresponding DN values of the windows  $m_{ij}$  and  $w_{ij}$  (from which the mean DN values for the respective windows was subtracted) and by summations over all lines and samples,  $i,j$ :

$$c_0 = \sum w_{ij} * m_{ij} \quad (4a)$$

$$c_1 = \sum m_{ij} * m_{ij} \quad (4b)$$

$$c_2 = \sum w_{ij} * w_{ij} \quad (4c)$$

The correlation coefficients  $c$  for each window position were stored in data arrays, in which the position of the star was determined by searching for local maxima. The coordinates of this maximum were determined with subpixel accuracy. From the right ascension and declination of the stars in the catalog, we computed the expected line/sample coordinates of these stars using the nominal pointing data available for each image. These were compared with the star positions from the automated star search. Normally, 50-80% of the stars in the chart, falling within the area of the respective image, were successfully correlated with stars in the images.

In the following, the precise positions of the stars were compared with the catalog. A least-squares program was developed to determine the camera focal length and the precise pointing of the image in terms of boresight right ascension, declination, and twist on the basis of the identified stars. The nominal image pointing parameters were used as a first guess to start the iterations. The 1- $\sigma$  value of the residuals of the star positions after these fits are shown in Table 4. While  $\sigma = 1.07$  pixels, on average, for the manual fits (second column), this value is effectively reduced to  $\sigma = 0.75$  for the automated matching (third column). The large  $\sigma (>1)$  for some of the manual measurements is probably due to misidentifications of stars. When the identification of stars is correct, the accuracy of the measurements is typically on the same order as that of the automated matching. When distinct signatures of smeared stars are available, the automated matching is clearly superior to the manual measurements (see image starcl131, Fig. 4). In cases of very heavy smear, however, in which star signatures overlap, the automated matching failed.

## 5.2 Distortion Model

The residuals were then examined for image distortion (see Fig. 6, left) and subjected to the laboratory distortion function (eqs. 1-3). The residuals are reduced from  $\sigma = 0.79$  to  $\sigma = 0.617$  (39.1%), a quite moderate improvement (Fig. 6, right). Alternatively, the laboratory function (Table 3) was used to correct the raw line/sample star positions using equations (1-3); then the fitting was repeated. The residuals after the fit are reduced to an average of  $\sigma = 0.47$  pixels, with some images showing residuals of as small as  $\sigma = 0.32$  (Table 4, rightmost column). This indicates that the characteristic distortion pattern found during the calibration on the ground can still be identified in the in-flight images; but obviously; the random noise in the star position measurements is large for some of the images. The camera focal length was found to be:  $f = 685.24 \pm 0.29$  mm (mean of all fits), a value which has a higher uncertainty and which is slightly smaller than the laboratory value of  $686.55 \pm 0.05$ . Both focal lengths are clearly above the nominal value of 677 mm.

In the next step, an attempt was made to determine a new distortion model from the in-flight data to identify possible changes in the camera geometric properties after spacecraft launch. All residuals after the individual fits were combined and new polynomial coefficients was fitted, as was done for the laboratory images. The initial residuals with  $\sigma = 0.791$  were reduced to  $\sigma = 0.525$  after the fit. Thus, the laboratory model accounts for 56% of the scatter in the data. Although this new model seems to be a better fit than the laboratory model, tests suggest that the two sets of coefficients probably differ only because of the random errors in the data. Random errors in the line/sample position measurements are clearly larger than in the calibration images ( $\sigma = 0.354$ ).

Table 4: 1 -  $\sigma$  residuals after least-squares fit

Image File	Manual Measurements	Automated Measurements	Autom. Measurements after geom. correction
starcl013	1.1633 [15]	0.9018 [18]	0.6265
starcl021	0.7952 [16]	0.7970 [19]	0.3516
starcl071	0.8417 [15]	0.9097 [24]	0.6206
starcl091	1.2454 [16]	0.8844 [27]	0.5683
starcl141	0.8812 [14]	0.9809 [31]	0.6136
starcl131	0.9322 [19]	0.7936 [26]	0.3932
starcl151	0.9356 [16] *)		
starcl191	0.9071 [16]	0.6885 [22]	0.3268
starcl201	1.2976 [18] *)		
nav04110	2.2501 [8]	0.5707 [8]	0.3456
nav04112	5.4750 [12]	1.0577 [6]	1.0238
nav04113	0.8481 [22]	0.9317 [19]	0.5628
nav04210	0.9254 [9]	0.6075 [14]	0.4356
nav04212	1.0809 [13]	0.8478 [13]	0.4617
nav04213	0.8353 [21]	0.6735 [14]	0.4688
nav04308	0.9462 [12]	0.7266 [13]	0.3443
nav04309	0.8798 [22]	0.3711 [19]	0.3871
nav04408	0.8682 [13]	0.4257 [12]	0.4461
nav04409	0.9188 [21]	0.5150 [13]	0.4270
Mean**)	1.07	0.75	0.47

Numbers in brackets give the number of identified stars

\*) automated matching failed (very smeared images with overlapping star trails)

\*\*) root mean square (after eliminating obvious outliers)

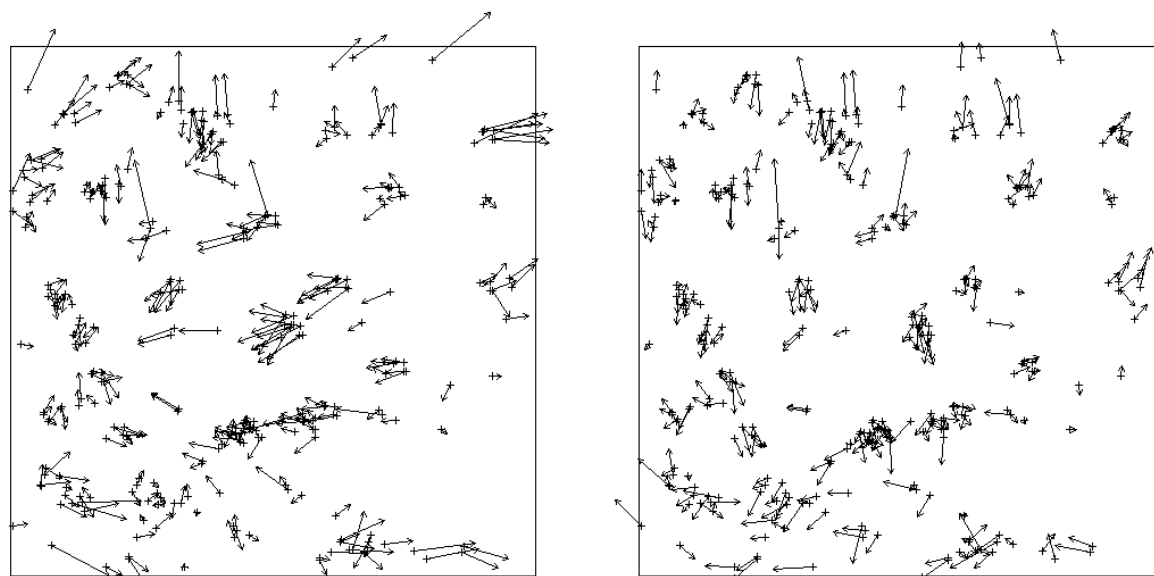


Fig. 6: Vector plots showing offsets between nominal and measured position of stars in the 1024 x 1024 image. Data from all 19 star images were combined. The plot shows data residuals before (left) and after (right) the best-fit distortion model (equations 1-3, Table 3) is applied. Compare magnitude and overall shape of the distortion pattern before and after the fit with the laboratory data in Fig. 3. The stars are unfortunately not evenly distributed over the image area. The lengths of the arrows are exaggerated by a factor of 50, as in Fig. 3.

## 6 SUMMARY AND DISCUSSION

We have carried out a comprehensive study of laboratory and in-flight image data to study the geometric properties of the MICAS CCD sensor on the DS1 mission. Laboratory data show that there is significant image distortion in the MICAS CCD on the order of 2-4 pixels near the image margins. A polynomial model can successfully "explain" approx. 80% of the observed scatter in the data and can be used to geometrically correct the images. The laboratory focal length of the camera is determined to be  $f = 686.55 \pm 0.05$  mm, clearly above the nominal value of 677 mm. For given bore sight vectors, positions of features in the entire image can be predicted to better than 0.5 pixels ( $1 \sigma$ ) after this correction. Our analysis of the available in-flight image data shows that –within the errors of the analysis– the camera geometric properties essentially have not changed.

We find that the laboratory data gives a very solid basis for studies of camera geometric properties. In fact, it would have been more difficult to determine an image distortion model on the basis of the few and noisy star observations of this study alone. The laboratory data also can be analyzed more rapidly than the star images. We estimate that the analysis of the laboratory data took 20% of the time required for the star image analysis.

Owing to the strong geometric distortion and the limited ability to correct for this effect, it is difficult to use the camera for precision photogrammetric analysis and for optical navigation purposes. There are several ways to improve this situation: More calibration images should be taken which should include more images in which the target is rotated. Availability of more images would make an automated analysis of the calibration images worthwhile. This may ultimately result in more sophisticated image distortion models represented by higher-order polynomials. Also, more star field images, should be taken with each of them showing more stars than are currently visible in the data. The current mounting of the camera on the DS1 spacecraft causes strong light scattering which makes it difficult to reliably detect faint stars. This unfortunate situation is expected to be improved when the camera is used in future space missions.

It would be desirable to study the MICAS camera design with the geometric calibration data in hand in order to find models based on physical grounds for the observed distortion patterns. Owing to the lack of such camera design data, the distortion function in this paper was derived by pure mathematical treatment of the observations. However, studies of the camera light path using ray tracing techniques are now beginning; first results indeed show that image distortions of the observed order of magnitude are typical for MICAS with its compact design and its required complicated light path (R. Kirk, Unites States Geological Survey, Flagstaff, pers. comm.). Precise analyses are to follow.

## ACKNOWLEDGMENTS

We wish to thank the members of the DS1 science team, in particular R. Nelson (science team lead, Jet Propulsion Laboratory, Pasadena, Ca) and L. Soderblom (MICAS team lead, United States Geological Survey, Flagstaff, Az) who contributed helpful discussions to this analysis. We are also very grateful to S. Bhaskaran and D. Thomas (both at JPL) who provided supporting information and data on the calibration of the MICAS camera.

## REFERENCES

- Nelson, R., Deep Space One: Preparing for Space Exploration in the 21st Cenury, EOS Trans. Vol 79, No. 41, p.493, 1998.
- Nelson, R., M. Rayman, P. Varghese, D. Bliss, D.H. Lehman, L.A. Soderblom, D.T. Young, F. Bagenal, D. Boice, D. Britt, R.H. Brown, B.J. Buratti, W. Ip, R. Meier, J. Oberst, T. Owen, B. R. Sandel, S.A. Stern, N. Thomas, J.J. Wang, R. Yelle, M.D. Hicks, J.K. Hillier, J.L. Piatek, and A.S. Hale, The New Millenium Deep Space One Mission, submitted to Space Science Reviews, 2000.
- Roser S. and U. Bastian, Positions and proper motions of 181731 stars north of -2.5 degrees declination for equinox and epoch J2000.0, Astron. Rechen-Institut, Heidelberg, 1989.
- Roser S. et al., Catalog of positions and proper motions of 197179 stars. Southern part. Astron. Rechen-Institut, Heidelberg, 1991.

APPENDIX

In addition to the calibration work by the DS1 science team, the navigation team at JPL (Jet Propulsion Laboratory), Pasadena, has carried out a geometric calibration of the CCD camera for their immediate use in optical navigation. In this appendix, the approach by the navigation team is described, and results are compared.

One important difference to our approach is that the navigation team used in-flight star images only to determine the camera's image distortion. However, more star images were used than was possible in this study. Contrary to the standard polynomial used in this paper, an alternative model function was used. True line and sample coordinates are computed from their nominal values by adding correction terms  $f_x(x,y)$  and  $f_y(x,y)$  to term, respectively, (cf. eqs. 1a, 1b) (S. Bhaskaran, JPL Navigation Team, pers. communication):

$$f_x(x,y) = \sum_i \sum_j p_{x_i} * p_{y_j} * c_{x_{ij}} \tag{A1a}$$

$$f_y(x,y) = \sum_i \sum_j p_{x_i} * p_{y_j} * c_{y_{ij}} \tag{A1b}$$

with

$$p_{x_0} = 1 \quad p_{x_1} = x \quad p_{x_i} = ((2i-1) * x * p_{x_{i-1}} - (i-1) * p_{x_{i-2}}) / i \tag{A2a}$$

$$p_{y_0} = 1 \quad p_{y_1} = y \quad p_{y_i} = ((2i-1) * y * p_{y_{i-1}} - (i-1) * p_{y_{i-2}}) / i \tag{A2b}$$

and with  $x$  and  $y$  as defined in equations (3a, 3b). The  $c_{x_{ij}}$  and  $c_{y_{ij}}$  are coefficients to be determined.

We applied this model and determined the Legendre polynomial coefficients by least-squares fits to our measured laboratory and in-flight data (see Table 5) to verify that the model is adequate to describe the image distortion. The residuals after the fit to the laboratory data are reduced from  $\sigma = 0.828$  to  $\sigma = 0.348$  pixels; the total sum of squares is reduced by 82.3% (standard polynomial: 81.7%; see Table 6 for a summary). For the in-flight star images, the model reduces the  $\sigma = 0.791$  to  $\sigma = 0.622$ , by just 38.2% (standard polynomial: 39.1%). Hence, the performance of this model function is similar, although it has more parameters than our standard polynomial.

Table 5: Coefficients of Legendre Polynomial Model determined from laboratory data

i	j	$c_{x_{ij}}$	$c_{y_{ij}}$	i	j	$c_{x_{ij}}$	$c_{y_{ij}}$
0	0	0.03718	0.29545	2	0	0.22187	1.84231
0	1	-0.36544	0.29275	2	1	0.13639	1.24594
0	2	-0.07886	1.54224	2	2	-0.14216	-0.02451
0	3	0.08650	0.60204	2	3	-0.02549	0.26160
1	0	0.18991	-0.19642	3	0	0.64703	0.06169
1	1	-0.03023	0.33829	3	1	0.35777	0.05198
1	2	1.39967	0.10587	3	2	0.18976	-0.04531
1	3	-0.41903	0.06525	3	3	-0.00445	-0.05422

Next, the modelling results of the navigation team, as expressed by the coefficients of the Legendre polynomial (which were made available to us, S. Bhaskaran, pers. communication) were compared with our distortion model. We consider our image grid measurements to be the best data set in terms of noise. However, the "navigation model" fits only moderately well to these data ( $\sigma = 55.8, 54.6\%$ ). The focal length was determined to be 684.695 mm (S. Bhaskaran, pers. communication), slightly smaller than both of our estimates, but closer to our in-flight value (685.24) than to the laboratory value (686.55). Comparison of the two distortion patterns by visual inspection (see Fig. 7) reveals an overall agreement between the two models, with the navigation model being more symmetric in shape (Fig. 7, right). However, there are noted differences near the image margins. Again, one might raise the question whether the geometric properties of the camera have slightly changed during the mission.

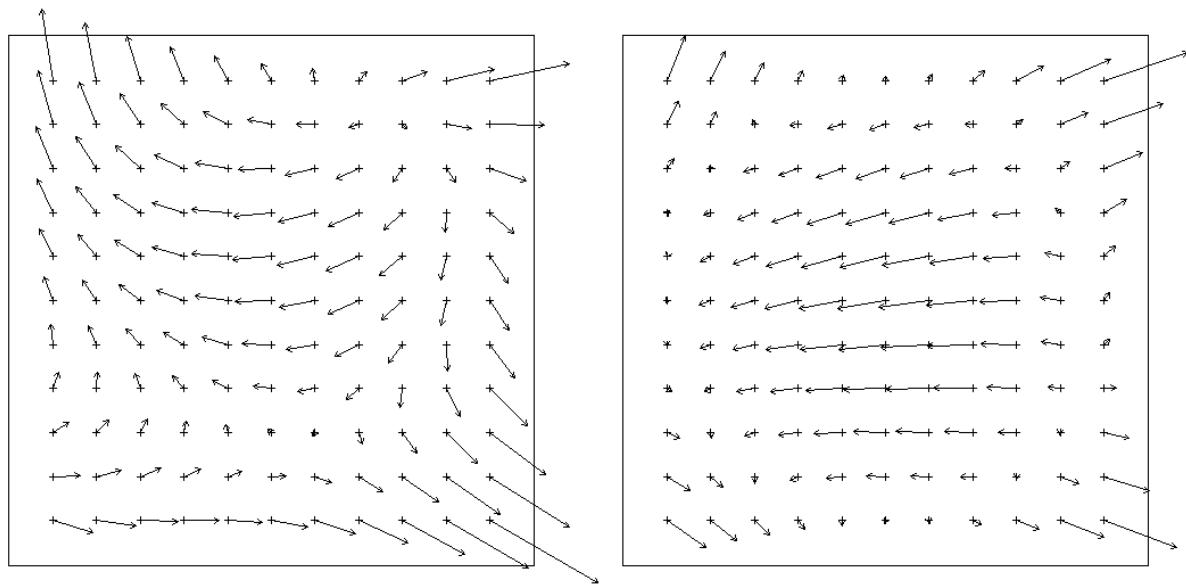


Fig. 7: The standard polynomial distortion model, derived in this study (left), compared with the Legendre polynomial model by the DS1 navigation team (right). There is good agreement regarding the magnitude and overall pattern of the image distortion. Notable differences exist near the image margins (see text for details). Compare the two models with the patterns of the residual data in Figs. 3 (left) and 6 (left).

The navigation model performs similar to the standard polynomial when applied to our star position measurements:  $\sigma = 0.620$  (38.6%). In contrast, the navigation model achieved an overall fit of  $\sigma = 0.361$  ( $\sigma = 0.342$  and  $\sigma = 0.116$  in the vertical and in the line direction, respectively) to their own twice as large set of star position measurements (S. Bhaskaran, pers. communication). (This data set included 41 images and a total of 389 star position measurements, which apparently do not suffer from noise as much as ours). We suggest that both in-flight models differ because of the random noise in the in-flight data. The comparison of the two independently derived models reminds us of the limits in our modelling efforts and suggests that any distortion corrections for the MICAS CCD near the image margins are to be considered with scrutiny.

Table 6: Summary:  $1 \sigma$  of the data residuals (pixels) and removal of data scatter (%) for laboratory and in-flight calibration using Standard and Legendre polynomial functions

Laboratory:	Raw Data	Standard Polynomial	Legendre Polynomial
	0.828	0.354 (81.7%) #)	0.348 (82.3%) ##) *) 0.558 (54.6%) ***)
Star Images:	0.79	0.525 (56%) 0.617 (39.1%)	0.509 (58.5%) *) 0.622 (38.2%) **) 0.620 (38.6%) ***)

#) See coefficients in Table 3      ##) See coefficients in Table 5  
 \*) Fit to the data  
 \*\*) Using the polynomial coefficients from the laboratory calibration  
 \*\*\*) Using the polynomial coefficients from the navigation team (Legendre only)